

Detecting eclipsing double white dwarfs with electromagnetic and gravitational waves

Hong-Ming Jin,¹ Bo Ma,^{2,3} Yong Shao,⁴ and Yan Wang^{1*}

¹MOE Key Laboratory of Fundamental Physical Quantities Measurements, Department of Astronomy and School of Physics, Huazhong University of Science and Technology, Wuhan 430074, P. R. China

²School of Physics and Astronomy, Sun Yat-sen University, Zhuhai 519082, P. R. China

³CSST science Center in the Great Bay Area, Zhuhai 519082, P. R. China

⁴Department of Astronomy, Nanjing University, Nanjing 210023, P. R. China

Accepted XXX. Received YYY; in original form ZZZ

ABSTRACT

Galactic double white dwarfs are predominant sources of gravitational waves in the millihertz frequencies accessible to space-borne gravitational wave detectors. With advances in multi-messenger astronomy, an increasing number of double white dwarf systems will be discovered through both electromagnetic and gravitational wave observations. In this paper, we simulated two populations of double white dwarfs originating from different star formation histories (hereafter referred to as Model 1 and Model 2) using the binary population synthesis method. We predicted the number of double white dwarfs in our Galaxy detectable by TianQin and Laser Interferometer Space Antenna (LISA) individually, as well as through their joint observation. In addition, we performed an analysis to evaluate the accuracy of the parameter estimation using the Fisher information matrix. Furthermore, we predicted the number of eclipsing double white dwarfs detectable by Gaia and LSST. Our study found that over the nominal mission durations, TianQin, LISA, and their joint observation can detect 5×10^3 (1×10^4), 1.7×10^4 (3.3×10^4), and 1.8×10^4 (3.5×10^4) double white dwarfs with signal-to-noise ratios greater than 7 in Model 1 (Model 2), respectively. Gaia and LSST are expected to detect 67 (186) and 273 (554) eclipsing double white dwarfs in Model 1 (Model 2) with orbital period less than 30 hours, respectively. We also found that several dozen eclipsing double white dwarfs can be detected jointly through electromagnetic and gravitational wave observations.

Key words: gravitational waves: double white dwarfs.

1 INTRODUCTION

White dwarfs (WDs) are the final evolutionary stage of main sequence stars with masses less than $8 - 10 M_{\odot}$ (Icko Iben et al. 1997; Dobbie et al. 2006). Based on our current understanding of stellar evolution and initial mass distribution, it is estimated that more than 95% of main sequence stars in our Galaxy will evolve into WDs (Baker et al. 2019; Gentile Fusillo et al. 2021a). These stars can no longer produce energy through nuclear fusion reactions, and as a result, they will gradually cool down over time by radiating their stored thermal energy, eventually becoming fainter. The evolution of WDs is reasonably well understood, with further details available in previous reviews (D’Antona & Mazzitelli 1990; Fontaine et al. 2001; Althaus et al. 2010).

A significant fraction of stars in our Galaxy exist in binary systems (Sana et al. 2012; Duchêne & Kraus 2013; El-Badry et al. 2021b). Observation shows that the binary fraction is greater than 0.5 for stars with masses $> 1 M_{\odot}$ (see van Haften et al. 2013, Appendix A). Toonen et al. (2017) simulated a sample of WDs within

20 pc of Earth using a population synthesis method and predicted that optically resolvable double white dwarfs (DWDs) constitute 9–14% of the population. Previous simulations using binary population synthesis have suggested that there are about 10^8 DWDs in our Galaxy (Nelemans et al. 2001b; Yu & Jeffery 2010; Breivik et al. 2020a). With the advances of multi-messenger astronomy, a wealth of observations on WD binaries will be pivotal in exploring the evolution of binary stars (Postnov & Yungelson 2014), refining the parameters in binary population synthesis models, such as the efficiency parameter of common envelope evolution (Dewi & Tauris 2000; Hirai & Mandel 2022; Chen et al. 2024). In addition, these observations contribute to the exploration of the mechanisms underlying Type Ia supernovae (Toonen et al. 2012) and to the study of the structure of our Galaxy (Rowell & Hambly 2011; Korol et al. 2019).

Observing WDs is challenging due to their inherently low luminosities. However, the total number of WD candidates has steadily risen with the ongoing progress of large-scale automated surveys and the accumulation of data. The latest WD catalog from Gaia Early Data Release 3 (EDR3) contains about 359,000 high-confidence WD candidates (Gentile Fusillo et al. 2021b). Through a spectroscopic survey focusing on $< 0.3 M_{\odot}$ He-core WDs, the Extremely

* E-mail: ywang12@hust.edu.cn (YW)

Low Mass (ELM) survey has discovered 98 detached DWDs (Brown et al. 2020). Follow-up spectroscopy and high-speed photometry observations have confirmed a growing number of DWDs, such as ZTF J153932.16+502738.8 (Burdge et al. 2019), ZTF J0538+1953, ZTF J2029+1534, ZTF J0722+1839, ZTF J1749+0924 (Burdge et al. 2020a), ZTF J2243+5242 (Burdge et al. 2020b), ZTF J1901+5309 (Coughlin et al. 2020), and LAMOST J0140355+392651 (El-Badry et al. 2021a).

Eclipsing binary systems can provide a better opportunity to measure the parameters of both companion stars. We summarized over a dozen known eclipsing DWDs in Table A1 in Appendix A. Based on Gaia’s WD catalog and data from the Zwicky Transient Facility (ZTF), 17 new eclipsing binaries have been identified (Keller et al. 2022), among which the majority are the WD binaries with a main-sequence companion, with only two possibly containing an extremely low-mass WD companion. Utilizing the Gaia EDR3 catalog and ZTF light curve data, Ren et al. (2023) identified a sample of 429 close WD binary candidates through a systematic search for short-period binaries. Wells et al. (2017) quantitatively validated the detection capability of Legacy Survey of Space and Time (LSST; LSST Science Collaboration et al. 2009) for eclipsing binaries by simulating a pseudo-LSST sample of binary light curves and subsequently recovering their periods from the light curves. The results indicate that the periods of 71% binary targets in the sample could be successfully recovered. As the data from Gaia and ZTF continue to accumulate and with the future operation of the 10-year multi-purpose optical survey of LSST, an increasing number of DWDs will be discovered.

On the other hand, in the era of gravitational wave (GW) astronomy, DWDs are one of the most promising sources for proposed space-borne laser interferometers, such as the Laser Interferometer Space Antenna (LISA; Amaro-Seoane et al. 2017), TianQin (Luo et al. 2016), Taiji (Hu & Wu 2017), ASTROD-GW (Ni 1998), and gLISA (Tinto et al. 2015). Tens of thousands of DWDs in our Galaxy could be detected by these GW detectors (Nelemans et al. 2001a; Marsh 2011; Ruiter et al. 2010; Korol et al. 2017; Lamberts et al. 2019; Huang et al. 2020). Binary systems that have been confirmed by EM observations and are expected to be detected by future GW observations are defined as verification binaries (VBs). Kupfer et al. (2018) collected catalogs of known VBs and identified 11 VBs with a signal-to-noise ratios (SNRs) greater than 20, two additional VBs with SNRs of at least 5, and three additional VBs projected to archive SNRs of approximately 5 following a 4-year mission duration of LISA. Burdge et al. (2020a) conducted a systematic search of the ZTF data and identified 15 binary systems with orbital periods ranging from 6.91 to 56.35 minutes. Among these, 5 sources have SNR greater than 5 for a 4-year mission duration of LISA. For joint GW observations, it was found that the spatial localization and characterization of binaries can be improved by combining data from multiple detectors, including LISA, TianQin, and Taiji (Gong et al. 2021; Wu & Li 2023).

While more than one hundred DWD systems have been discovered so far by electromagnetic (EM) observations, there is a noticeable selection bias. This bias arises from the fact that DWDs with higher luminosities and closer distances to the observer are more likely to be detected by EM observations. However, to study the population characteristics of DWDs in our Galaxy, we need a more comprehensive sample. Binary population synthesis (BPS) is the conventional method for studying the evolution of binary populations and has wide applications in astrophysics. To date, a variety of BPS codes have been developed, such as SeBa (Portegies Zwart & Verbunt 1996; Nelemans et al. 2001a), Yunnan Model (Han 1998; Han et al. 2002, 2003; Zhang et al. 2002, 2004), BSE (Hurley et al. 2002), COSMIC

(Breivik et al. 2020b), and COMPAS (Riley et al. 2022). Binary population synthesis produces statistical samples of certain types of stars for subsequent astrophysical investigations. For example, it has been used to explore the number of detectable DWDs in our Galaxy for LISA (Toonen et al. 2017; Korol et al. 2020). Huang et al. (2020) investigated the ability of TianQin to detect DWDs in our Galaxy using a synthetic catalog from Toonen et al. (2012, 2017), which shows that about 8.7×10^3 DWDs can be detected over the 5-year nominal mission duration of TianQin. Finch et al. (2023) found that prior EM-derived knowledge of VBs can improve the accuracy of GW parameter estimation in the Bayesian framework. The formation and evolution of ultra-compact X-ray binaries (UCXBs) in the Galactic bulge has been explored using SeBa simulations by van Haften et al. (2013). Renzo et al. (2021) investigated the potential of LISA to detect of GWs from inspiraling binaries in common envelope phases using COSMIC. Lau et al. (2020) used a double neutron star (DNS) population generated by COMPAS to estimate the properties of DNS systems with cumulative SNRs greater than 8 during the 4-year LISA mission. Using a modified BSE code, Shao & Li (2021) predicted that LISA could detect dozens of GW sources with stellar-mass black holes in our Galaxy.

In this paper, we used the Compact Object Synthesis and Monte Carlo Investigation Code (COSMIC; Breivik et al. 2020b), a publicly available Python-based population synthesis software¹, to generate comprehensive samples of DWDs in our Galaxy. We simulated two populations of DWDs based on different star formation histories (hereafter referred to as Model 1 and Model 2). We find that the number of detectable DWDs with GWs or EM waves is 2–3 times higher in Model 2 than in Model 1. We simulated the light curves of DWDs in the Gaia *G*-band and LSST (*ugrizy*) bands using the Physics Of Eclipsing BinariEs (PHOEBE; Prša 2018). Our simulations show that the LSST-*r* band performs best compared to the other bands. For future multi-messenger observations of DWDs, we predict the differences in the parameter distributions of DWDs detectable with GW and EM observations. We find that EM observations are more likely to detect DWDs with longer periods and closer distances compared to GWs.

The structure of this paper is as follows. In Section 2, we introduce the population synthesis method used to generate DWD populations in our Galaxy. In Section 3, we simulate the light curves of eclipsing DWDs and investigate their detectability in the photometric surveys of Gaia and LSST. In Section 4, we estimate the number of DWDs that are detectable by LISA, TianQin, and their joint observations. In addition, we evaluate the accuracy of the parameter estimation for these DWDs. In Section 5, we discuss the results of the joint observations of DWDs with GW and EM observations. The paper is concluded in Section 6.

2 POPULATION SYNTHESIS OF DWDs

In this section, we discuss the settings of initial parameters, the choices of binary evolution models, and the Galactic structure when conducting binary population synthesis simulations for the DWDs in our Galaxy.

¹ <https://cosmic-popsynth.github.io/docs/stable/>

Table 1. Science requirements for Gaia and LSST. The referenced parameters are from [Gaia Collaboration et al. \(2016a\)](#) and [Ivezić et al. \(2019\)](#), respectively.

	Gaia	LSST
Survey Area	whole sky	20000 deg ²
Single Visit Limiting Magnitude	21	<i>u</i> : 23.9; <i>g</i> : 25; <i>r</i> : 24.7; <i>i</i> : 24; <i>z</i> : 23.3; <i>y</i> : 22.1
Total visits per sky patch	70	<i>u</i> : 56; <i>g</i> : 80; <i>r</i> : 184; <i>i</i> : 184; <i>z</i> : 160; <i>y</i> : 160
Wavelength coverage	330–1050 nm	320–1050 nm (<i>ugrizy</i>)
Nominal mission lifetime	5yr	10 yr

2.1 Initial parameters

We initiate a population of zero-age main-sequence (ZAMS) stars by employing the probability distribution functions for their initial parameters. Subsequently, we evolve this initial population using a specific evolutionary model which leads to the formation of a sample of DWDs. The initial values for the parameters of the binaries are derived by sampling the distribution functions related to the initial metallicity (Z), primary mass (m), binary mass ratio (q), orbital separation (a), eccentricity (e), and orbital inclination angle (i). COSMIC has several built-in options for the distribution functions of the initial parameters, such as the initial mass functions: ‘Salpeter55’ ([Salpeter 1955](#)), ‘Kroupa93’ ([Kroupa et al. 1993](#)), ‘Kroupa01’ ([Kroupa 2001](#)), or user-defined power-law exponents; the initial orbital separation distribution functions: log-uniform ([Abt 1983](#)), ‘Sana2012’ ([Dominik et al. 2012](#)), ‘Renzo2019’ ([Renzo et al. 2019](#)); the initial eccentricity distributions: the thermal distribution ([Heggie 1975](#)), the uniform distribution ([Geller et al. 2019](#)). In our simulations, the initial mass function follows [Kroupa et al. \(1993\)](#) with a mass range of $0.08 - 150 M_{\odot}$, the binary mass ratio q adopts the uniform distribution between $[0, 1]$, the orbital separation (in unit of solar radius) is sampled from the log-uniform distribution with $\log(a)$ between $[0, 6]$, and the eccentricity adopts the thermal distribution with e between $[0, 1]$. We use a constant binary fraction of 0.5 and a constant metallicity of 0.02.

To investigate the impact of star formation history on binary system evolution, we simulate two populations of DWDs that share the same initial parameters described in the previous paragraph except for their star formation histories. In Model 1, we adopt a burst of star formation 13.7 Gyr ago ([Yu & Jeffery 2010](#)). In Model 2, we follow the star formation history in [Wagg et al. \(2022\)](#), which assumes a constant star formation rate over 10 Gyr for the thin disk, a 1 Gyr burst of star formation 11 Gyr ago for the thick disk, and a 1 Gyr burst of 10 Gyr ago for the bulge.

Due to limited computational resources, we only simulate a subset with a fixed number of DWDs. This sample will be scaled up to represent the entire population with N_{Galaxy} DWDs, and

$$N_{\text{Galaxy}} = N_{\text{fixed}} \frac{M_{\text{Galaxy}}}{M_{\text{fixed}}}. \quad (1)$$

Here, N_{fixed} denotes the number of DWDs in the fixed subset, M_{fixed} denotes the mass of the ZAMS stars used to produce this fixed subset, and M_{Galaxy} represents the mass of the different structures of our Galaxy. N_{Galaxy} is the number of DWDs in the corresponding structures of our Galaxy. Following the composition of the Galaxy structure of [McMillan \(2011\)](#), we divide our Galaxy into bulge, thin disk, and thick disk, with total masses of each component of $8.9 \times 10^9 M_{\odot}$, $4.32 \times 10^{10} M_{\odot}$ and $1.44 \times 10^{10} M_{\odot}$, respectively. In Model 1, we calculate the total number of DWDs, N_{Galaxy} , by

scaling the number (N_{fixed}) of DWDs generated by bursts of the star formation history. In Model 2, we calculate the total number of DWDs ($N_{\text{Galaxy_Bulge}}$, $N_{\text{Galaxy_Thindisk}}$, $N_{\text{Galaxy_Thickdisk}}$) by scaling the numbers of DWDs ($N_{\text{fixed_Bulge}}$, $N_{\text{fixed_Thindisk}}$, $N_{\text{fixed_Thickdisk}}$) generated by three star formation histories for the bulge, thin disk and thick disk in Model 2. For the entire sample, we scale up the fixed subsets by conducting random sampling with replacement (allowing sampling of the same source more than once) from the fixed subsets.

2.2 Galactic structure

The position of the DWD in our Galaxy is essential for calculating the flux of the light curve (Sec. 3.1) and the signal-to-noise ratio (SNR) of the GW signals (Sec. 4.1). Here, we assume that the structure of our Galaxy is axisymmetric, and assign a position to each pair of DWDs by sampling the distribution of the mass densities in different Galactic structures. Previous work usually assumed an exponential squared bulge and a squared hyperbolic secant plus an exponential disk or a double exponential disk ([Nelemans et al. 2004](#); [Yu & Jeffery 2010](#); [Korol et al. 2019](#)). A comprehensive summary of the Galactic models widely employed in the literature is provided in [Nissanke et al. \(2012\)](#). In this work, we adopt the density profile for the bulge described in [McMillan \(2011\)](#):

$$\rho_{\text{b}}(R, z) = \frac{\rho_{\text{b},0}}{(1 + r'/r_0)^{\alpha}} \exp\left[-(r'/r_{\text{cut}})^2\right] M_{\odot} \text{ kpc}^{-3}, \quad (2)$$

where the cylindrical polar coordinate R is the radial distance and z is the height. $r' = \sqrt{R^2 + (z/q_1)^2}$, $q_1 = 0.5$, $\alpha = 1.8$, $r_0 = 0.075$ kpc, $r_{\text{cut}} = 2.1$ kpc, and $\rho_{\text{b},0} = 9.93 \times 10^{10} M_{\odot} \text{ kpc}^{-3}$.

The Galaxy’s disk is composed of a thin and a thick part, each with a double-exponential density profile with different scale lengths and scale heights,

$$\rho_{\text{d}}(R, z) = \frac{\Sigma_{\text{d},0}}{2z_{\text{d}}} \exp\left(-\frac{|z|}{z_{\text{d}}} - \frac{R}{R_{\text{d}}}\right) M_{\odot} \text{ kpc}^{-3}. \quad (3)$$

For the thin disk, the scale height is $z_{\text{d}} = 0.3$ kpc, the scale length is $R_{\text{d}} = 2.9$ kpc, and the central surface density is $\Sigma_{\text{d},0} = 816.6 M_{\odot} \text{ pc}^{-2}$. For the thick disk, the scale height is $z_{\text{d}} = 0.9$ kpc, the scale length is $R_{\text{d}} = 3.31$ kpc, and the central surface density is $\Sigma_{\text{d},0} = 209.5 M_{\odot} \text{ pc}^{-2}$. For the Sun-Galactic center distance, we adopt $R_0 = 8.178$ kpc ([GRAVITY Collaboration et al. 2019](#)).

2.3 Simulated DWDs

As mentioned above, we generate N_{fixed} DWDs as a fixed subset using different star formation histories for Model 1 and Model 2. To ensure adequate sampling of the short period end of DWDs, with periods of approximately several minutes, a relatively large N_{fixed} is necessary. After several trial experiments, we decided to set $N_{\text{fixed}} = 1.7 \times 10^8$. We then scaled up the simulated fixed population of DWDs to represent the entire population expected in our Galaxy.

In addition to the intrinsic physical parameters discussed in Sec. 2.1, we need to assign values for the extrinsic geometric parameters to each pair of DWDs. Specifically, R and z are drawn according to Eq. 2 and Eq. 3 for the bulge and disk, respectively. The azimuth angle ϕ is drawn from the uniform distribution between $[0, 2\pi]$. We transform (R, z, ϕ) to the Ecliptic, Galactocentric, ICRS coordinates to get ecliptic longitude, ecliptic latitude, distance (lon , lat , d), Galactic longitude, Galactic latitude, distance (l , b , d), Right ascension, Declination, distance (RA, Dec, d) for the convenience of the next steps. Here d represent the distance between the DWD and the observer.

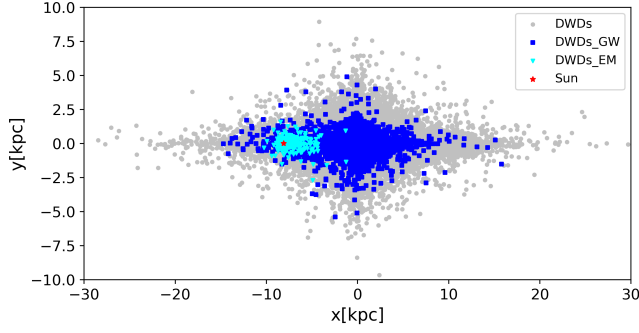


Figure 1. Distribution of DWDs in the $x - z$ plane of the Galactic Cartesian coordinate system. Grey squares represent a small representative subset of the simulated Galactic DWDs. Blue squares represent DWDs detectable by TianQin ($\text{SNR} > 7$), and cyan squares represent DWDs detectable by Gaia and LSST.

The cosine of the orbital inclination i follows a uniform distribution between $[0, 1]$. Since the detection frequency of DWDs relevant to space-borne GW detectors is mainly in the millihertz range, we select DWDs with orbital periods of less than 30 hours for further analysis. In the end, we obtained final populations of Galactic DWDs with orbital periods less than 30 hours in Model 1 and Model 2, which amount to 6.8×10^7 and 4.454×10^7 , respectively. In Figure 1, we show the distribution of a small representative subset of the simulated DWDs (grey squares) in our Galaxy, along with the ones detectable by EM and GW observations (see details in Section 3 and 4.).

3 EM OBSERVATION

In this section, we utilize PHOEBE (the PHysics Of Eclipsing BinariEs; Prša 2018; Prša & Zwitter 2005; Prša et al. 2016; Horvat et al. 2018; Jones et al. 2020; Conroy et al. 2020) to generate light curves for the simulated DWDs in Section 2 and investigate the detection capabilities of DWDs based on the photometric performance of Gaia and LSST.

The Gaia mission was launched in December 2013 and has since been in operation for over 10 years (Gaia Collaboration et al. 2016a). To obtain the most comprehensive information about our Galaxy, Gaia scans the entire sky and measures astrometry, photometry, radial velocities, and many astrophysical characteristics for billions of stars. Gaia has released several datasets containing approximately 1.8 billion sources brighter than 21 so far (Gaia Collaboration et al. 2016b, 2018, 2021, 2022). These progressive data releases have seen impressive growth in the identification of white dwarf candidates within the catalog, increasing from 73,221 to 359,000 (Jiménez-Esteban et al. 2018; Gentile Fusillo et al. 2019, 2021b).

The Vera C. Rubin Observatory is expected to start the Legacy Survey of Space and Time (LSST) in 2025. LSST will produce an abundance of images and data products that will contribute to exploring our solar system, galaxy, and universe over ten years of mission. The telescope will observe the southern celestial hemisphere (about 20000 square degrees) in six broad-band (*ugrizy*) filters covering the wavelength range of 320 to 1050 nm. As the principal component of LSST, the main wide-fast-deep (WFD) survey will pay about 825 visits to each 9.6 square degree field summed over all six bands (LSST Science Collaboration et al. 2017; Bianco et al. 2021; Schwamb et al. 2023). For this study, we have employed simulated 10-year survey pointing databases generated by the Operation Simulator (OpSim;

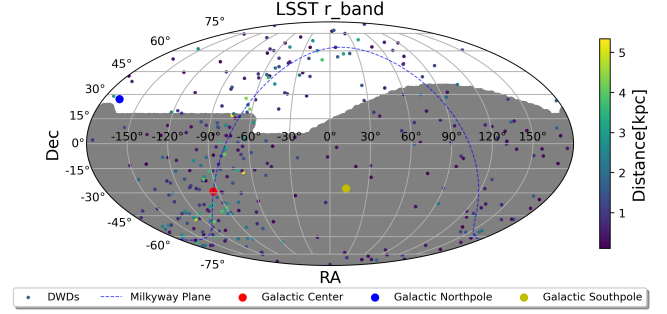


Figure 2. Distribution of detectable eclipsing DWDs in the LSST r -band across the celestial sphere from our simulation. The sky is shown in an equal-area Mollweide projection in equatorial coordinates (R.A. is increasing from left to right). The gray area indicates the sky region covered by LSST r -band.

Naghieb et al. 2019; Delgado & Reuter 2016; Delgado et al. 2014) on NOIRLab’s Astro Data Lab¹ to get the regions of the sky covered by LSST. The shaded area in Figure 2 represents the sky coverage of the LSST- r band.

3.1 Light curve simulation

PHOEBE can produce and fit light curves and radial velocity profiles of eclipsing binaries. In light curve simulation, the input parameters for the binary include: r_1 , r_2 , T_1 , T_2 , a , d , P , i , and e , where r_1 and r_2 are the radii and T_1 and T_2 are the effective temperatures of each white dwarf, a is the orbital semi-major axis, d represents the distance of the DWD from the observer, P is the orbital period, i is the orbital inclination, and e is the orbital eccentricity. In addition to the primary influence of these intrinsic parameters on the light curve, we also consider secondary effects, such as limb-darkening and mutual irradiation effects. The limb-darkening coefficient is automatically obtained by interpolating the applicable tables based on the atmospheric parameters for ease of calculation (Prša et al. 2016). For the mutual irradiation effects, we adopt the default irradiation method ‘horvat’ (Horvat et al. 2019). However, we have not considered the surface distortion due to tides and rotation (ellipsoidal variation) in this work. Finally, we convert the output flux measured in W/m^2 to apparent magnitudes for various bands in Gaia, LSST, and include the Gaussian noise from observational uncertainties and the extinction effect due to interstellar dust in our synthetic light curves.

According to the definition of Casagrande & VandenBerg (2018), Gaia magnitude is defined as

$$G_\zeta = -2.5 \log \bar{I}_\zeta + ZP_\zeta, \quad (4)$$

where \bar{I}_ζ is the weighted mean flux in a given band ζ (G_{BP} , G_{RP} , G) expressed in photoelectrons per second. This conversion from energy flux to photon flux follows the procedure outlined in Gaia DR2 documentation (Chapter 5; van Leeuwen et al. 2018). ZP_ζ represents the photometric zero point for a given band. We calculate the Gaia G -band magnitude in the VEGAMAG system referring to the latest ZP_{VEG} value of 25.6874, as presented in Table 3 of Riello et al. (2021). We use the photometric standard error of a single visit:

$$\sigma_G [\text{mag}] = 1.2 \times 10^{-3} \left(0.04895z_x^2 + 1.8633z_x + 0.0001985 \right)^{1/2},$$

¹ <https://datalab.noirlab.edu/>

Table 2. Summary of entire DWD population in different Galactic components. He represents helium WD, CO represents carbon-oxygen WD, and ONe represents oxygen–neon–magnesium WD. ONe + WD represents the DWD in which one star is an ONe WD and the other is a WD of any type.

Component	DWD type	N_{total} (P<30h) Model 1	N_{total} (TQ) (SNR>7)	N_{total} (LISA) (SNR>7)	N_{total} (P<30h) Model 2	N_{total} (TQ) (SNR>7)	N_{total} (LISA) (SNR>7)
Bulge	He + He	4.76×10^6	355	1347	3.37×10^6	345	1321
	CO + He	3.16×10^6	291	829	2.22×10^6	282	875
	CO + CO	1.20×10^6	26	38	9.76×10^5	4	13
	ONe + WD	6.64×10^4	3	4	6.59×10^4	11	23
Thin disk	He + He	2.31×10^7	1676	6747	7.35×10^6	2692	10095
	CO + He	1.54×10^7	1475	4150	9.74×10^6	4480	12946
	CO + CO	5.82×10^6	104	207	6.20×10^6	954	2838
	ONe + WD	3.21×10^5	11	24	5.23×10^5	271	633
Thick disk	He + He	7.70×10^6	529	2211	7.61×10^6	650	2561
	CO + He	5.12×10^6	469	1350	4.47×10^6	480	1471
	CO + CO	1.94×10^6	25	46	1.92×10^6	2	16
	ONe + WD	1.08×10^5	5	7	1.28×10^5	9	23
	total	6.87×10^7	4969	16960	4.45×10^7	10180	32815

Table 3. The GW amplitude \mathcal{A} and SNR of 16 optical candidates of eclipsing DWDs. TianQin and LISA employ a nominal mission duration of four and five years, respectively.

Name	\mathcal{A}	SNR (TQ)	SNR (LISA)	SNR (TQ + LISA)
GALEX J1717 + 6757	1.02177×10^{-22}	0.008403	0.014482	0.017160
NLTT 11748	8.605459×10^{-23}	0.011357	0.016871	0.020962
CSS 41177	5.467304×10^{-23}	0.02776843	0.08581914	0.09105031
SDSS J0751 + 0141	2.702653×10^{-23}	0.047547	0.102344	0.114835
SDSS J1152 + 0248	1.035830×10^{-22}	0.032169	0.241741	0.244296
J2102 + 4145	1.007×10^{-22}	0.060802	0.423346	0.428553
SDSS J0822 + 3048	7.471462×10^{-23}	0.934605	1.938355	2.192093
ZTF J1901 + 5309	8.238431×10^{-23}	0.639979	2.019739	2.137936
J0225 + 6920	1.491916×10^{-23}	0.394455	3.006700	3.037594
ZTF J1749 + 0924	5.703240×10^{-23}	1.261504	3.557513	3.816500
ZTF J2029 + 1534	4.528334×10^{-23}	1.119049	5.094065	5.239500
ZTF J0722 + 1839	1.130579×10^{-22}	4.958398	9.199127	10.682861
ZTF J2243 + 5242	7.414352×10^{-23}	6.601330	59.705461	60.141825
ZTF J1539 + 5027	9.926494×10^{-23}	15.567999	71.519980	73.524889
SDSS J0651 + 2844	1.509569×10^{-22}	21.621458	74.632938	78.300715
ZTF J0538 + 1953	2.385216×10^{-22}	29.080216	88.316568	93.885755

(5)

where $z_x = \max \left[10^{0.4(12-15)}, 10^{0.4(G-15)} \right]$ (Gaia Collaboration et al. 2016a).

According to LSST Science Collaboration et al. (2009), we calculate the LSST magnitude in the AB magnitude system, expressed as follows:

$$m_\zeta \equiv -2.5 \log_{10} \left(\frac{F_\zeta}{F_{AB}} \right), \quad (6)$$

where F_ζ corresponds to the flux in a given band ($\zeta = ugrizy$) in units of Jansky ($1 \text{ Jansky} = 10^{-26} \text{ W Hz}^{-1}$ and $F_{AB} = 3631 \text{ Jy}$). The photometric error for a point source in a single visit can be written as

$$\sigma_L^2 = \sigma_{\text{sys}}^2 + \sigma_{\text{rand}}^2, \quad (7)$$

where the systematic photometric error $\sigma_{\text{sys}} = 0.005 \text{ mag}$ and the random photometric error $\sigma_{\text{rand}}^2 = (0.04 - \gamma)x + \gamma x^2 \left(\text{mag}^2 \right)$ with $x = 10^{0.4(m-m_5)}$. m_5 is the 5σ depth (for point sources) in a given band. The values of the parameters can be found in Table 3.2 of LSST Science Collaboration et al. (2009).

We adopt the distance-dependent extinction model defined in Breivik et al. (2018) for the DWDs distributed in the Galactic disk and bulge.

In the disk, the extinction in the V band

$$A_V(d)_{\text{disk}} = A_V(\infty) \tanh \left(\frac{d \sin(b)}{z_h} \right), \quad (8)$$

where d is the distance, b is the galactic latitude and the scale height $z_h = 0.3 \text{ kpc}$.

In the bulge,

$$A_V(d)_{\text{bulge}} = A_V(\infty) \text{Erf} \left(\frac{d \sin(b)}{R_h} \right), \quad (9)$$

where $R_h = 0.5 \text{ kpc}$ and $\text{Erf}(\cdot)$ is the error function. $A_V(\infty)$ is defined in Nelemans et al. (2004) as follows:

$$A_V(\infty) = \begin{cases} 0.165 \frac{[\tan(50^\circ) - \tan(b)]}{\sin(b)} & \text{for } b < 50^\circ, \\ 0 & \text{for } b \geq 50^\circ. \end{cases} \quad (10)$$

We transform the V -band extinction to the Gaia G -band and the LSST ($ugrizy$) bands according to

$$A(\lambda) = A_V(a(\bar{x}) + b(\bar{x})/R_V), \quad (11)$$

where $R_V = 3.1$ for our Galaxy. The coefficients $a(\bar{x})$ and $b(\bar{x})$ are functions of wavelength ($\bar{x} = 1/\lambda$), and A_V is the extinction in the V band for disk or for bulge (Cardelli et al. 1989).

Using the above equations, we simulate the light curves of eclipsing DWDs observable by Gaia and LSST. In Figure 3, we show the

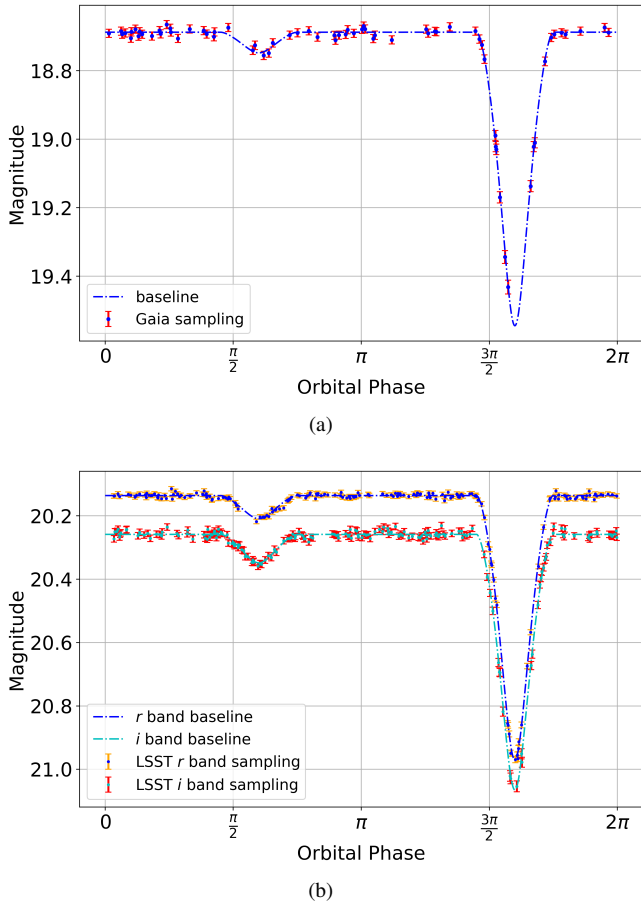


Figure 3. Simulated light curves of an eclipsing DWDs in the Gaia G -band (top panel), the LSST- r and $-i$ bands (bottom panel). Dash-dotted lines represent the simulated noiseless light curves. The number of simulated Gaia and LSST photometric data points are taken from Table 1.

simulated light curves for an eclipsing DWD using the following parameters: $r_1 = 0.02980 R_\odot$, $r_2 = 0.0275 R_\odot$, $T_1 = 26300$ K, $T_2 = 9200$ K, $a = 0.1227 R_\odot$, $d = 1.6$ kpc, $P = 0.1466$ h, and $i = 82^\circ$. The primary eclipse is clearly visible in the simulated light curves.

3.2 Source selection

From all simulated DWDs, we select detectable eclipsing DWDs in the Gaia and LSST surveys using criteria that include the survey limiting magnitudes, the target coordinates, the chi-square χ^2 tests of the light curves, and the inclination angles of the DWDs.

For Gaia, we select DWDs that are brighter than magnitude 21 over the entire sky. For LSST, we select DWDs based on the sky coverage and the limiting magnitude of each bandpass. The sky map of LSST is shown in Figure 2, and the limiting magnitudes for each bandpass are listed in Table 1. To ensure the selected binaries are eclipsing, we also apply the criterion of $\cos i \leq (r_1 + r_2)/a$, where i , r_i , a are the orbital inclination, radii of WDs, and orbital separation, respectively.

To distinguish eclipsing DWDs from non-variable stars with photometric fluctuations, we used a method similar to that of Korol et al.

Table 4. The number of detectable eclipsing DWDs in our Galaxy by Gaia and LSST in our simulations. For LSST, we list the number of detection for each bandpass in the LSST filters (*ugrizy*), as well as the total number obtained when combining all bandpasses (the second last column). We also derive the total number of detections when combining observations from Gaia and LSST (the last column).

	Gaia	LSST						total	total
		<i>u</i>	<i>g</i>	<i>r</i>	<i>i</i>	<i>z</i>	<i>y</i>		
Model 1	67	16	189	247	116	55	1	273	289
Model 2	186	38	429	488	228	107	3	554	623

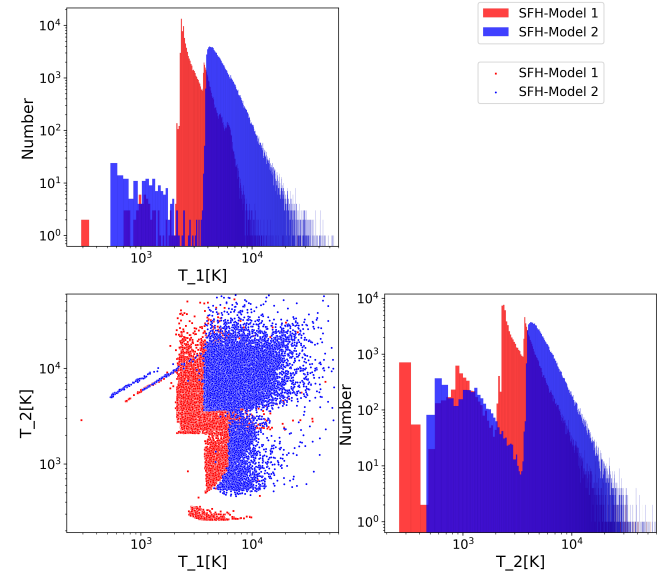


Figure 4. Corner plots for the temperatures of the primary (T_1) and companion (T_2) stars of DWDs from simulations in Model 1 (red) and Model 2 (blue) of star formation history.

(2019) to select DWDs with $\chi^2 > 3$. Here,

$$\chi^2 = \frac{1}{N} \sum_{i=1}^N \left(\frac{G_i - G_{\text{mean}}}{\sigma_i} \right)^2, \quad (12)$$

where N is the total number of visits per star given in Table 1, G_i represents the measured photometric magnitude from each visit, σ_i represents the photometric error as stated in Equations 5 and 7, and G_{mean} represents the mean photometric magnitude for all visits in the same bandpass. Based on the above selection criteria, the numbers of detectable eclipsing DWDs in our simulations are counted and summarized in Table 4.

3.3 Results

In Table 4, we show the number of eclipsing DWDs detectable by Gaia and LSST in both Model 1 and Model 2. Our results show that 67 and 273 DWDs produced in Model 1 can be detected by Gaia and LSST, respectively. In Model 2, these numbers increase to 186 and 554, respectively. The primary factor contributing to the difference between Model 1 and Model 2 is the choice of the star formation history as described in Section 2, which results in different temperature distributions for the simulated populations of DWDs as

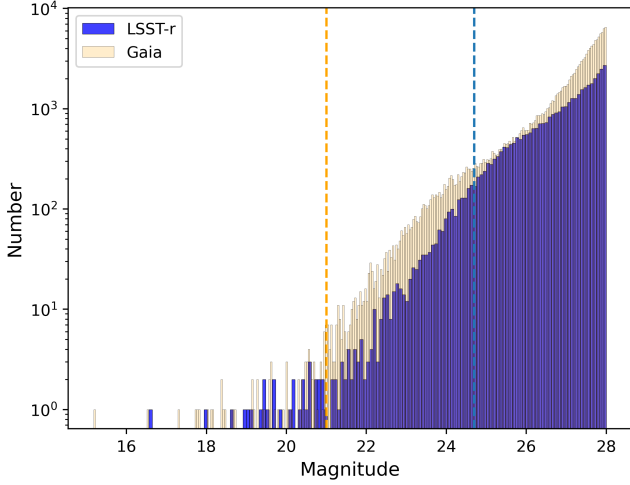


Figure 5. Distributions of the apparent magnitudes of the eclipsing DWDs in Model 1. The light orange and blue histograms represent samples from the Gaia G -band and the LSST- r band, respectively. The orange and blue vertical dash lines represent the limiting magnitudes of the Gaia G -band and the LSST- r band, respectively.

shown in Figure 4. Due to the longer period of cooling timescale, the DWDs from Model 1 have overall lower temperature distributions for the primary and companion stars and are therefore less likely to be observed compared to those from Model 2. The distributions of apparent magnitudes for the corresponding DWDs are shown in Figure 5. As we can see, only a small fraction of the DWDs fall within the limiting magnitude, which is consistent with the results reported by Nelemans (2009).

Figure 6 shows the distributions of the main parameters of the DWDs detectable by the Gaia and the LSST- r band for Model 1. According to the distribution of Galactic latitude, about 70% of the DWDs are located within the ± 20 degree range of the Galactic plane. In the equatorial coordinate system, compared to the Gaia’s all-sky observations, the DWDs from the LSST observations are mainly located in the southern sky region. From the magnitude distribution, we can see that the magnitude increases with increasing distance. The peak of the magnitude distribution of the DWDs observed by LSST is around 22, which is slightly higher than that of Gaia. The distribution of distances shows that the DWDs detectable by LSST are mainly within 4 kpc and those detectable by Gaia are mainly within 2 kpc. As we can see from Figure 1 and Section 4, the space-borne GW detectors will have a greater distance reach than these optical telescopes, and therefore can detect more DWDs in our Galaxy. For the EM observations, extinction is a critical factor in the calculation of the apparent magnitude. According to Eqs. 10–11, extinction is mainly determined by the Galactic latitude, distance, and structure of the Galaxy. The closer the DWDs are to the Galactic plane, the stronger the extinctions. The distance of the DWDs from the observer and the extinction show a proportional linear relationship; the greater the distance from the DWDs, the stronger the extinction.

Figure 7 illustrates the sky distributions of 67 (273) eclipsing DWDs in Model 1 that are detectable by Gaia and LSST. Our results show that LSST can detect 273 eclipsing DWDs in Model 1 and 554 in Model 2. These numbers are lower than those reported by Korol et al. (2019) (hereafter referred to as K19), which are 1100 and 1475 for two different models. Several factors account for this discrepancy. The major factor is the calculation of errors of apparent

magnitude of the WDs. K19 effectively uses σ_{rand}^4 instead of σ_{rand}^2 in Eq. 7, which leads to an underestimation of the photometric errors, especially for fainter WDs. In our validation tests, using σ_{rand}^4 for the random photometric errors allows LSST to detect 998 DWDs in Model 1 and 1815 in Model 2, which are more consistent with the numbers reported in K19. In addition, our simulation of the light curves for each LSST bandpass ($ugrizy$) is based on the number of sampling points (visits) listed in Table 1. In contrast, K19 considers only the LSST- r band and assigns 1000 sampling points to it. The other minor factors include different star formation histories, initial mass functions, and the masses and mass density distributions of the Galactic disk and bulge adopted in our study.

4 GW OBSERVATION

In this section, we simulate the GW signals from the DWDs obtained in Section 2.3 and calculate their SNRs for TianQin, LISA, and their joint observation. In addition, we evaluate estimation accuracy for the parameters of the DWDs using the Fisher information matrix (FIM).

4.1 GW signals

The GWs emitted by a DWD can be calculated using the quadrupole-moment formula (Peters & Mathews 1963), which are characterized by two polarizations:

$$h_+(t) = \mathcal{A} \left(1 + \cos^2 \iota \right) \cos \left(2\pi f t + \pi \dot{f} t^2 + \phi_0 + \Phi_D(t) \right), \quad (13a)$$

$$h_\times(t) = 2\mathcal{A} \cos \iota \sin \left(2\pi f t + \pi \dot{f} t^2 + \phi_0 + \Phi_D(t) \right). \quad (13b)$$

Here, the overall amplitude can be written as

$$\mathcal{A} = \frac{2(GM)^{5/3}}{c^4 d} (\pi f)^{2/3}, \quad (14)$$

and the time derivative of GW frequency f is

$$\dot{f} = \frac{96}{5} \frac{f}{M} (\pi f M)^{8/3}. \quad (15)$$

The chirp mass $M \equiv (m_1 m_2)^{3/5} / (m_1 + m_2)^{1/5}$, m_1 and m_2 are the component masses. The GW phase evolution in Eq. 13 includes initial phase ϕ_0 and Doppler modulation $\Phi_D(t)$. The latter can be expressed as follows:

$$\Phi_D(t) = 2\pi f \frac{R_0}{c} \sin \theta \cos(2\pi f_m t - \phi), \quad (16)$$

where $R_0 \approx 1.5 \times 10^8$ km is the distance between the Earth and the Sun, $f_m = 1/\text{year}$ is the modulation frequency, (θ, ϕ) are the ecliptic coordinates of the source. The GW strain signal measured by a detector can be expressed as:

$$h(t) = F^+(t)h_+(t) + F^\times(t)h_\times(t). \quad (17)$$

Here, $F^+(t)$ and $F^\times(t)$ are the detector’s antenna pattern functions which depend on the source’s location and its orientation relative to the detector. We adopt the expressions of the detector’s antenna pattern functions for TianQin from Hu et al. (2018); Huang et al. (2020), and for LISA from Cornish & Larson (2003). The squared SNR of the signal can be calculated as follows (Finn 1992)

$$\rho^2 = \frac{2}{\tilde{S}_n(f_0)} \int_0^T dt h(t)^2, \quad (18)$$

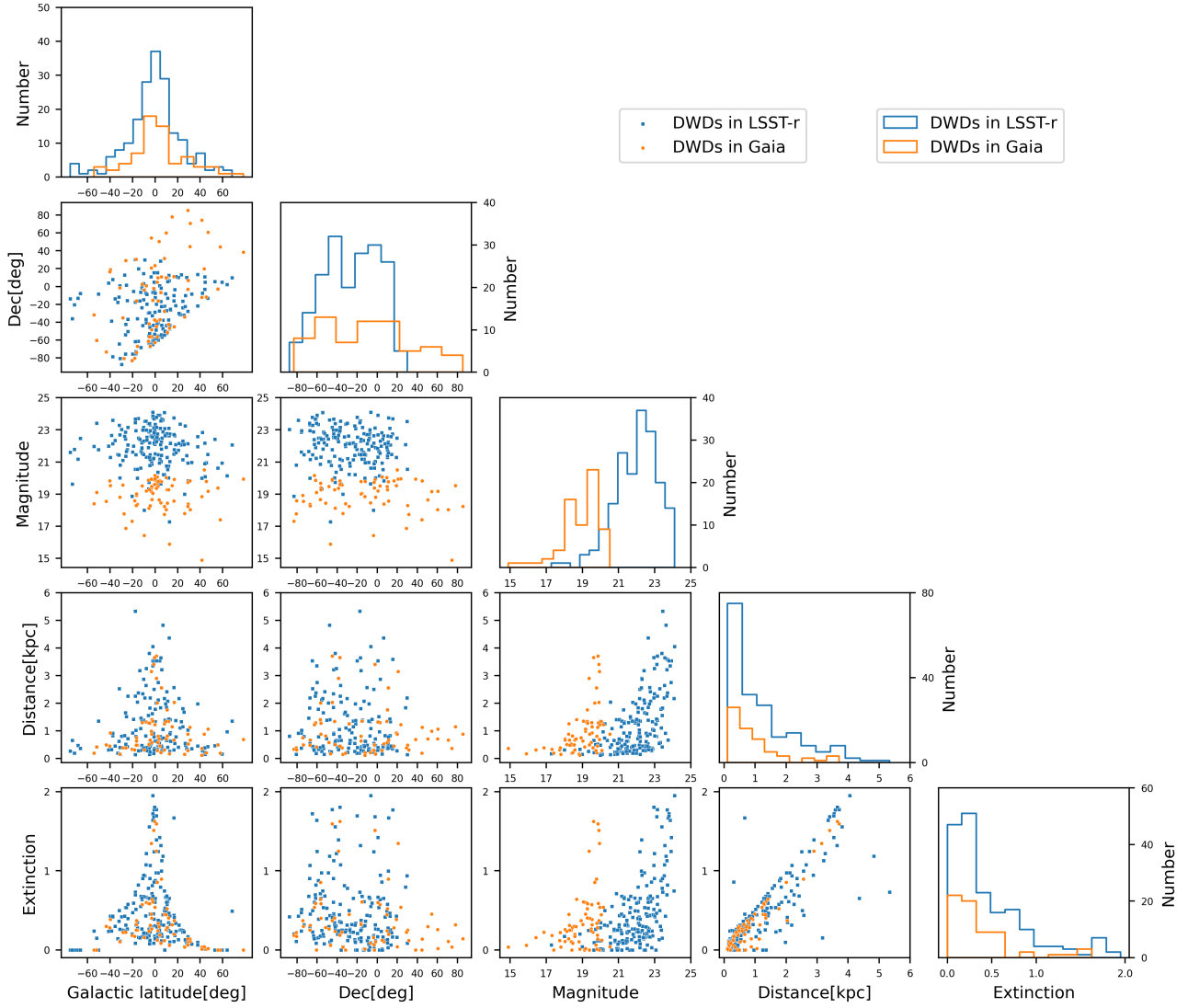


Figure 6. The corner plot for several parameters of eclipsing DWDs in the Gaia and LSST-*r* band samples. The diagonal histograms show the distributions of the Galactic latitude, Declination (Dec), apparent magnitude, distance, and extinction. The scatter plots show the correlations between each pair of parameters.

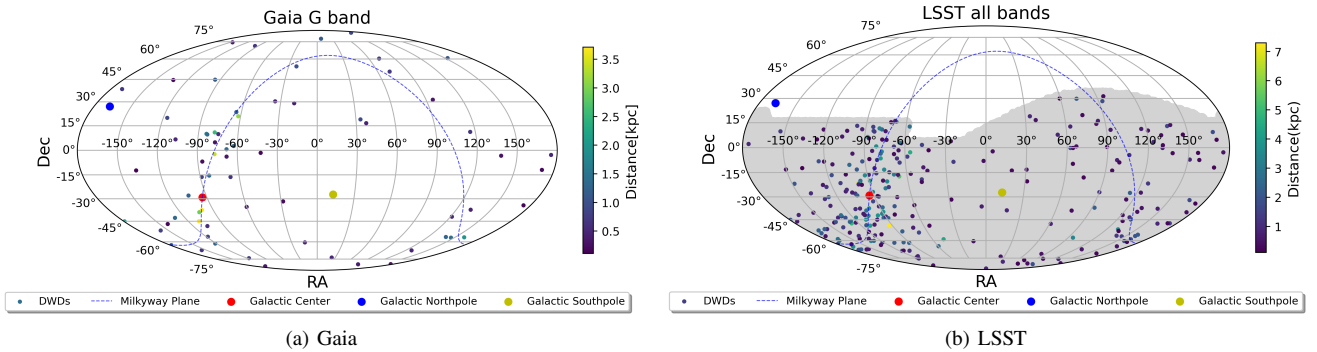


Figure 7. Sky distributions of the eclipsing DWDs (Model 1) detectable by Gaia (left panel) and LSST (right panel).

where $\tilde{S}_n(f_0)$ is the single-sided power spectral density (PSD) of detector at GW frequency f_0 , and T is the effective observation time. The PSDs for TianQin and LISA can be found in [Hu et al. \(2018\)](#); [Huang et al. \(2020\)](#) and [Robson et al. \(2019\)](#), respectively.

The accumulation of SNR depends on the effective observation time T . For TianQin, we adopt an observation scheme of three months on and three months off over a nominal five-year mission duration, which corresponds to an effective observation time of 2.5 years ([Luo et al. 2016](#); [Huang et al. 2020](#)). For LISA, the current baseline employs a duty cycle of 0.75 over a nominal four-year mission duration, resulting in an effective observation time of 3 years ([Amaro Seoane et al. 2022](#)). Note that for combined observation, the SNRs for TianQin and LISA are added quadratically, since the noise are independent for the two detectors ([Tinto & de Araujo 2016](#)).

4.2 Fisher information matrix

For multi-messenger astronomy, particularly for the EM follow-up of the GW signals, it is crucial to forecast the estimation accuracy for the parameters of the detectable DWDs. To achieve this, we use the Fisher information matrix defined as ([Cutler & Flanagan 1994](#))

$$\Gamma_{ij} = \left(\frac{\partial h}{\partial \xi_i} \mid \frac{\partial h}{\partial \xi_j} \right), \quad (19)$$

where (\mid) denotes the noise-weighted inner product. ξ_i represents the i -th unknown parameter in the parameter set that includes $\mathcal{A}, \iota, \psi, \theta, \phi, f, \phi_0, \dot{f}$. The inverse of FIM is equal to the covariance matrix, $\Sigma_{ij} = \Gamma_{ij}^{-1}$. The diagonal element Σ_{ii} represents the variance of the estimation error for ξ_i , and the non-diagonal element Σ_{ij} represents the covariance of the estimation errors between ξ_i and ξ_j . Based on the error propagation equation, we estimate the error of the source sky position measurement, the relative error of the chirp mass, and the relative error of the distance with the following equations:

$$\Delta\Omega = 2\pi \left(\Sigma_{\theta\theta} \Sigma_{\phi\phi} - \Sigma_{\theta\phi}^2 \right)^{1/2}, \quad (20)$$

$$\frac{\Delta M}{M} = \sqrt{\left(\frac{11}{5} \frac{\Sigma_{ff}}{f} \right)^2 + \left(\frac{3}{5} \frac{\Sigma_{\dot{f}\dot{f}}}{\dot{f}} \right)^2 + \frac{33}{25} \left(\frac{\Sigma_{ff}}{f} \right) \left(\frac{\Sigma_{\dot{f}\dot{f}}}{\dot{f}} \right) \Sigma_{f\dot{f}}}, \quad (21)$$

$$\frac{\Delta \mathcal{D}}{\mathcal{D}} = \sqrt{\left(\frac{\Sigma_{ff}}{f} \right)^2 + \left(3 \frac{\Sigma_{\dot{f}\dot{f}}}{\dot{f}} \right)^2 + \left(\frac{\Sigma_{\mathcal{A}\mathcal{A}}}{\mathcal{A}} \right)^2}. \quad (22)$$

Note that DWDs are typically quasi-monochromatic sources in the mHz band, so not all DWDs in our simulation exhibit a measurable \dot{f} (or $\Sigma_{\dot{f}\dot{f}}$). Here we adopt the commonly used criterion $\dot{f} T^2 \rho > 1$ ([Adams et al. 2012](#)) to select sources for which we can obtain reliable results from Eqs. 21 and 22. If this criterion is not met, \dot{f} will be excluded from in the parameters to be estimated in our analysis.

4.3 Results

Table 6 lists the expected numbers of DWDs in Model 1 and Model 2 with $\rho \geq 7(5)$ for TianQin, LISA, and their joint observation. For TianQin, we consider nominal mission duration of 1, 2, and 5 years, which correspond to effective observation times of 0.5, 1, and 2.5

years, respectively. For LISA, we consider nominal mission duration of 1, 2, and 4 years, which correspond to effective observation times of 0.75, 1.5, and 3 years, respectively. For Model 1, TianQin can detect approximately 5×10^3 DWDs with SNRs greater than 7 in 2.5 years of effective observation time and LISA can detect approximately 1.7×10^4 DWDs with SNRs greater than 7 in 3 years of effective observation time. For Model 2, TianQin can detect approximately 1×10^4 DWDs with SNRs greater than 7 in 2.5 years of effective observation time, which is comparable to the results in [Huang et al. \(2020\)](#) based on a DWD population generated from SeBa ([Toonen et al. 2017](#)); LISA can detect approximately 3×10^4 DWDs with SNRs greater than 7 in 3 years of effective observation time, which is comparable to the results in [Korol et al. \(2019\)](#). The numbers for Model 2 are about twice as many DWDs as the ones for Model 1. This is mainly due to Model 2 generating more DWDs with frequencies in the millihertz. The joint observation of TianQin and LISA can detect an additional 2,000 DWDs compared to LISA alone.

From the top panel of Figure 8, we can see that the frequencies of the DWDs detectable by TianQin and LISA are predominantly in the range of $10^{-3} - 10^{-2}$ Hz. The frequency distribution of DWDs detectable by LISA (centered around 2.5×10^{-3} Hz) exhibits a slightly lower frequency peak compared to TianQin (centered around 3.5×10^{-3} Hz). This is primarily attributed to the lower sensitivity curve of LISA compared to TianQin for frequencies below 10^{-2} Hz, allowing LISA to detect a greater number of lower frequency DWDs. The bottom panel shows the sensitivity curves ($\sqrt{f \tilde{S}_n(f)}$) for TianQin and LISA. Among the 16 optical candidates of eclipsing DWDs (marked as stars), we found that 5 of them (marked as red stars) accumulate SNRs greater than 7 (as shown in Table 3) over a nominal 4-year mission duration of LISA.

Figure 9 shows the distributions of parameter estimation accuracy obtained through the FIM analysis for Model 2. Our result yields 3241 (32%), 9760 (29%), and 10356 (29%) DWDs with SNRs between 7 and 10 for TianQin, LISA, and their joint observation, respectively. Only 2% of the DWDs exhibit SNRs greater than 100 for these three detector configurations. In Table 5, we count the cumulative numbers and corresponding percentages of DWDs with parameter estimation relative errors less than 0.1, 0.2, and 0.5 for TianQin, LISA, and their joint observation in Model 2. It can be seen that the total number of relative errors less than 0.1 for each parameter ranges from 1769 to 12218, and the percentage ranges from 12% to 58%. In particular, the number of sources with relative errors less than 0.5 is twice as large as the number of sources with relative errors less than 0.1. The relative error for distance is larger compared to the other parameters. From Equation 22 and the distributions of $\Delta\mathcal{A}/\mathcal{A}$, $\Delta f/f$, and $\Delta\dot{f}/\dot{f}$ in Figure 9, we can see that the relative error in $\Delta\mathcal{D}/\mathcal{D}$ is mainly contributed by $\Delta\mathcal{A}/\mathcal{A}$. About 79% and 76% of the DWDs have relative errors in $\Delta\mathcal{A}/\mathcal{A}$ and $\Delta\mathcal{D}/\mathcal{D}$ greater than 1 for TianQin in Model 2. For the sky localization, the numbers of the DWDs with position errors $\Delta\Omega < 1 \text{ deg}^2$ (10 deg^2) are 1889 (4974), 4010 (13750), and 4722 (14746) for TianQin, LISA, and their combination, respectively. Given the fields of view of Gaia and LSST are 1.26 deg^2 and 9.6 deg^2 , respectively, these sources can be easily targeted by the EM follow-up observations.

In Figure 10, we show the cumulative distributions of the relative errors of chirp mass, distance, and sky location in Model 2. TianQin and LISA can individually detect 216 (543) and 283 (727) DWDs, respectively, with relative errors in $\Delta M/M$ of less than 0.001 in Model 1 (Model 2). However, for their joint observation, the number reaches 391 (907), an increase of 38% (24%) over LISA alone in Model 1 (Model 2). For $\Delta\mathcal{D}/\mathcal{D}$, TianQin and LISA can individually

Table 5. Number and percentage of cumulative distributions of the relative errors of the parameters less than 0.1, 0.2, 0.5 for TianQin, LISA and their joint observation in Model 2.

	< 0.1			< 0.2			< 0.5		
	TQ	LISA	TQ+LISA	TQ	LISA	TQ+LISA	TQ	LISA	TQ+LISA
$\Delta\mathcal{A}/\mathcal{A}$	2061 (20%)	6516 (20%)	7456 (21%)	4280 (42%)	14341 (43%)	15574 (44%)	6618 (65%)	22412 (68%)	23930 (69%)
$\Delta\dot{f}/\dot{f}$	4744 (47%)	8666 (28%)	9091 (27%)	6342 (63%)	12257 (40%)	12769 (37%)	8611 (85%)	19041 (61%)	19772 (58%)
$\Delta\cos\iota$	3375 (33%)	11062 (34%)	12218 (35%)	5015 (49%)	16755 (51%)	18026 (51%)	6946 (68%)	23349 (71%)	24920 (71%)
$\Delta\psi$	2635 (26%)	9282 (28%)	10206 (29%)	4063 (39%)	13725 (42%)	14841 (42%)	5648 (56%)	18948 (57%)	20255 (58%)
$\Delta\mathcal{M}/\mathcal{M}$	5898 (58%)	11169 (36%)	11704 (34%)	7698 (76%)	15800 (51%)	16400 (48%)	9443 (94%)	23734 (76%)	24650 (72%)
$\Delta\mathcal{D}/\mathcal{D}$	1769 (17%)	3931 (12%)	4599 (13%)	3446 (34%)	7645 (24%)	8317 (24%)	6000 (59%)	14829 (47%)	21570 (63%)

Table 6. The expected numbers of Galactic DWDs detectable by TianQin, LISA, and their joint observation with $\rho \geq 7(5)$ over various mission durations. The results for $\rho \geq 5$ are given for comparison with other works.

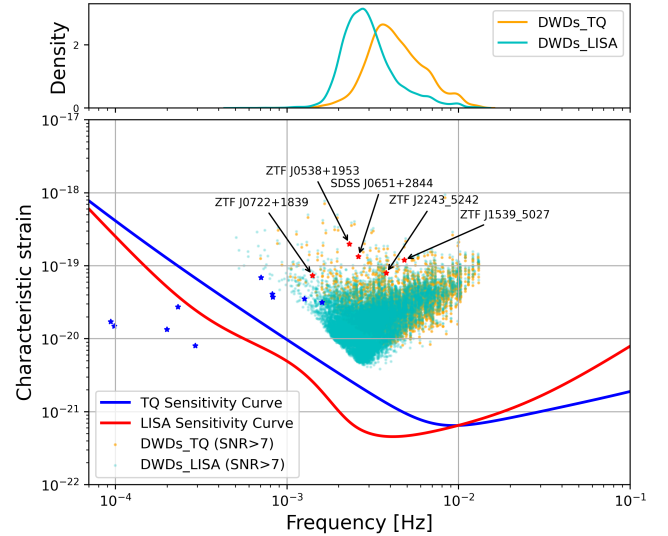
Detector	1yr	2yr	5yr
Model 1			
TianQin	2183 (3133)	3165 (4582)	4969 (7075)
LISA	5072 (6436)	6231 (8042)	16960 (23889)
TianQin+LISA	5482 (7012)	6923 (9144)	18087 (25548)
Model 2			
TianQin	4413 (6477)	6541 (9372)	10180 (14718)
LISA	9383 (12242)	12341 (15993)	32815 (44809)
TianQin+LISA	10380 (13765)	13888 (18346)	34917 (47832)

detect 915 (1769) and 1913 (3931) DWDs, respectively, with relative errors of less than 0.1 in Model 1 (Model 2). For their joint observation, the number reaches 2243 (4599), an increase of 17% (17%) over LISA alone in Model 1 (Model 2). For $\Delta\Omega$, TianQin and LISA can individually detect 926 (1889) and 1896 (4010) DWDs, respectively, with errors of less than 1 deg^2 in Model 1 (Model 2). For their joint observation, the number reaches 2275 (4722), an increase of 20% (18%) over LISA alone in Model 1 (Model 2). Overall, the numbers of the DWDs with errors $\Delta\mathcal{M}/\mathcal{M}$, $\Delta\mathcal{D}/\mathcal{D}$, and $\Delta\Omega$ of less than 0.001, 0.1, and 1 deg^2 , respectively, have approximately 20% increases in joint observation over LISA alone. Furthermore, combining EM observations will allow a more precise determination of the sky positions of the DWDs, which can facilitate the study of the structure of our Galaxy.

5 JOINT OBSERVATION

In the previous two sections, we examined separately the capabilities of Gaia and LSST in optical observations and the capabilities of TianQin and LISA in GW detections for the DWDs in our Galaxy. In this section, we examine the properties of the DWDs detectable by both GW and EM observations.

In Table 7, we show the numbers of the DWDs with SNRs greater than 7 in Model 1 and Model 2 during the 5-year and 4-year nominal mission durations for TianQin and LISA, respectively. In addition, we count the numbers of eclipsing DWDs, constrained by the criteria such as sky area, apparent magnitude, and chi-square test, within Model 1 and Model 2 during the 5-year and 10-year nominal mission lifetimes of Gaia and LSST, respectively. The numbers of DWDs detectable by either EM or GW observations in Model 2 are about 2-3 times larger than in Model 1. The detection of DWDs by GW is influenced by a number of factors, including the source distance, spatial position, mass, orbital period, and so forth. The main factor contributing to the differences in the numbers of GW detections

**Figure 8.** Bottom panel: The characteristic strain of the 15 optically observed eclipsing DWDs (indicated by blue and red stars), along with the characteristic strain of the simulated DWDs (cyan and orange dots) with $\rho > 7$ for TianQin and LISA as a function of frequency. The red and blue solid lines represent the sensitivity curves of LISA and TianQin respectively. Top panel: Frequency distributions of simulated DWDs with $\rho > 7$.

between Model 1 and Model 2 is the orbital period distribution of simulated DWDs. For example, in Model 2, the thin disk of our Galaxy follows a constant star formation history over a period of 10 billion years, resulting in more DWDs with frequencies in the millihertz range. On the other hand, we find that the main factor causing the difference in the numbers of EM detections between Model 1 and Model 2 is the effective surface temperature of the companion stars. We can see that the joint observation of TianQin and Gaia identifies 2 (Model 1) and 9 (Model 2) eclipsing DWDs. Similarly, the joint observation of TianQin and LSST identifies 7 (Model 1) and 11 (Model 2) eclipsing DWDs. In addition, the joint observation of LISA and Gaia identifies 4 (Model 1) and 29 (Model 2) eclipsing DWDs, while the joint observation of LISA and LSST identifies 15 (Model 1) and 47 (Model 2) eclipsing DWDs.

Figure 11 shows the distributions of distance, orbital period, and chirp mass of the DWDs detectable by EM and GW observations. From Figure 11(a), we can see that 95% of the Galactic DWDs detectable by GW detectors are within 12 kpc, while 95% of the eclipsing DWDs observed by optical telescopes are within 3.87 kpc. Their spatial distributions can be found in Figure 1. It is evident that the GW detectors can certainly make a more thorough survey of the DWDs in our Galaxy.

In Figure 11(b), we find that 97% of the DWDs detectable by GW

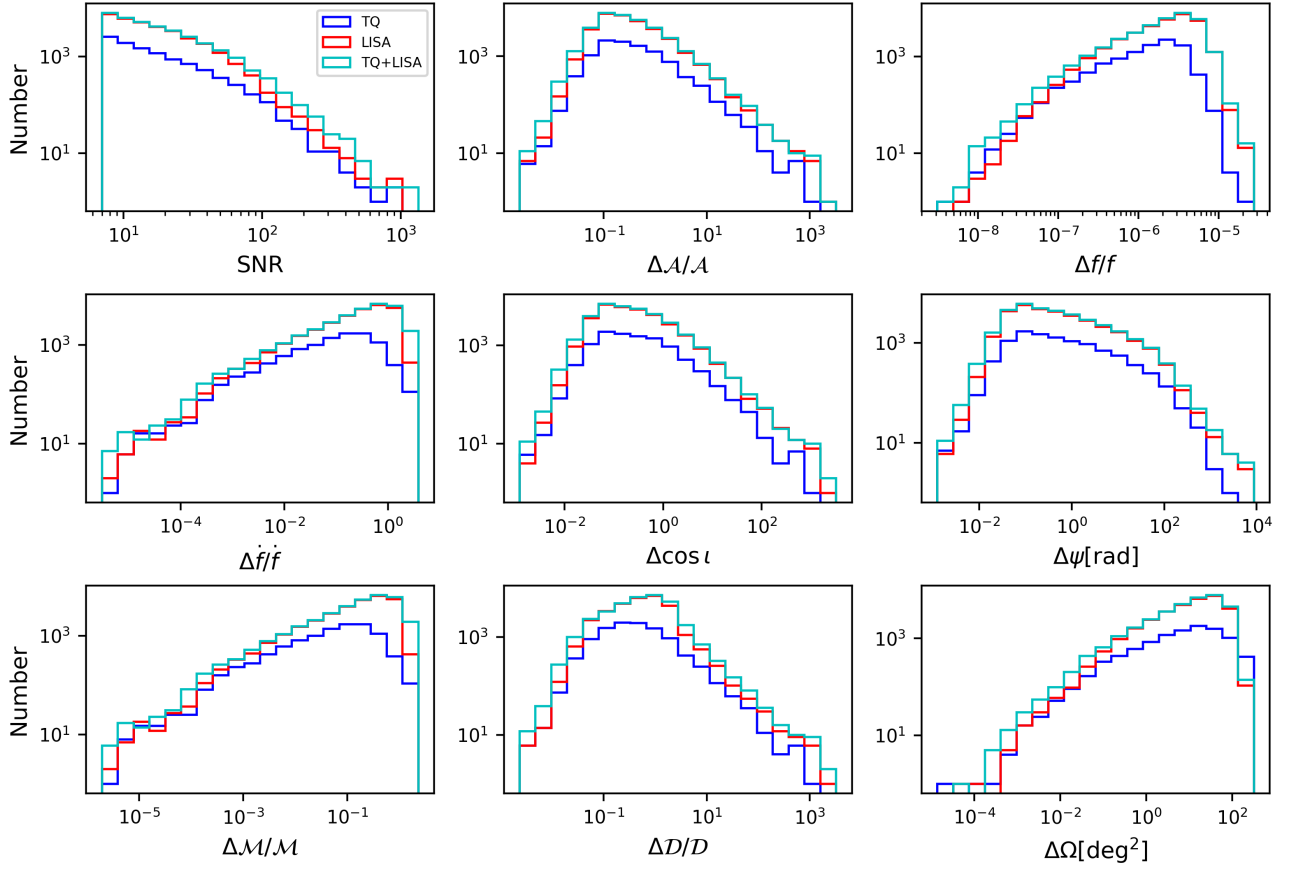


Figure 9. Histograms of the SNRs and parameter estimation accuracy of the DWDs detectable by TianQin, LISA, and their joint observation in Model 2.

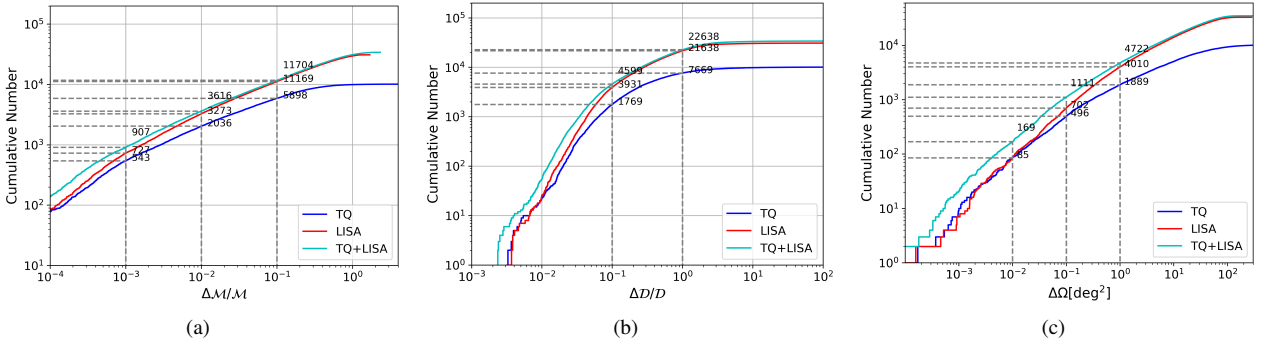


Figure 10. The cumulative distributions of the relative errors of (a) $\Delta M/M$, (b) $\Delta D/D$, and (c) $\Delta \Omega$ for the DWDs detectable by TianQin, LISA, and their joint observation in Model 2.

detectors have orbital periods shorter than 20 minutes. This is because the most sensitive frequency range of space-borne GW detectors is $10^{-3} - 10^{-2}$ Hz, which corresponds to orbital periods of 3 – 33 minutes. However, about only 2% of the DWDs in the entire population of our simulation have orbital periods shorter than 33 minutes. In contrast, 90% of eclipsing DWDs observed by optical telescopes have periods longer than 20 minutes. This partially explains why the number of DWDs jointly detectable by both GW detectors and optical telescopes is quite limited, and 90% of the DWDs have orbital periods between 8 and 25 minutes.

Figure 11(c) shows the chirp mass distributions, which peak

around $0.3 M_{\odot}$, with 76% of the DWDs distributed between $0.2 M_{\odot}$ and $0.4 M_{\odot}$ for the GW detectors. In terms of chemical composition, these DWDs are mainly He-CO and He-He DWDs, which is consistent with the case for the entire DWD population as shown in Table 2. It is also clear that the GW detectors can find heavier DWDs with masses greater than $0.5 M_{\odot}$ than the optical telescopes. On the other hand, WDs with a smaller mass typically have a larger radius, resulting in a larger radiating surface area. However, our analysis shows that compared to the radius, the surface temperature has a more significant effect on the optical detection of DWDs, which is actually a manifestation of the Stefan-Boltzmann law, $L = 4\pi R^2 \sigma T^4$,

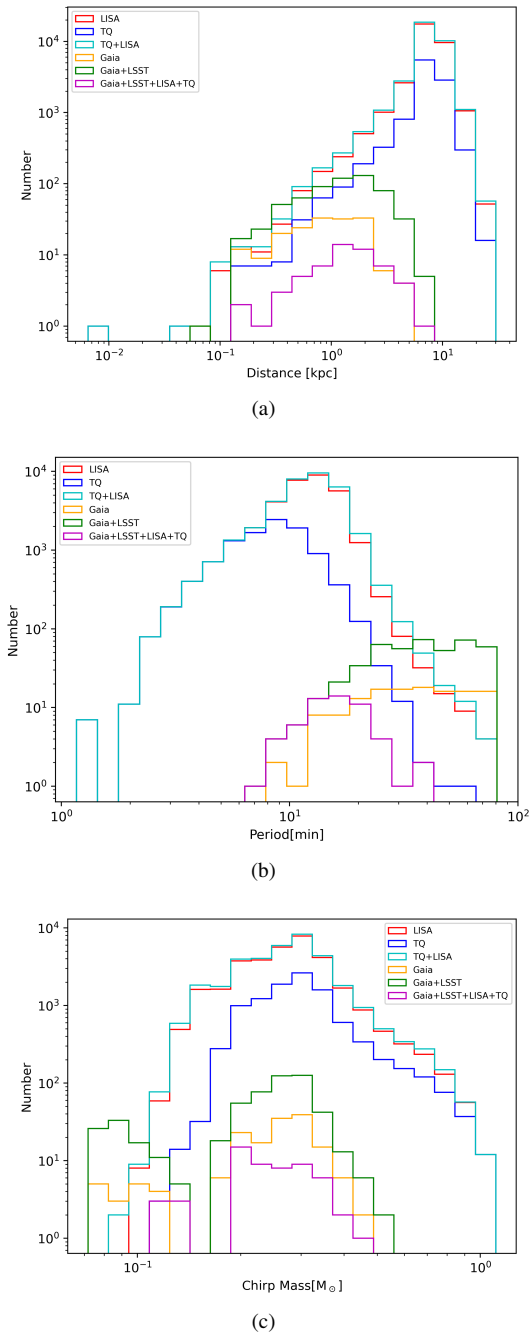


Figure 11. Histograms of source distance, orbital period, and chirp mass for different detector combinations.

where L is the radiation flux, R is the radius, and T is the surface temperature of the WD.

6 SUMMARY AND CONCLUSIONS

In this work, we simulated two populations of DWDs in our Galaxy with different star formation histories (Model 1 and Model 2) using binary population synthesis method. We predicted the numbers of DWDs detectable by TianQin, LISA, Gaia, and LSST individually and jointly in these two samples. We found that TianQin can detect 4969 (10180) DWDs with SNRs greater than 7 within a 5-year nominal

Table 7. Number of DWDs from Model 1 (Model 2) that are detectable by TianQin, LISA, Gaia, LSST individually (diagonal elements), and their joint observation (off-diagonal elements).

	TianQin	LISA	Gaia	LSST
TianQin	4969 (10180)	4969 (10180)	2 (9)	7 (11)
LISA	4969 (10180)	16960 (32815)	4 (29)	15 (47)
Gaia	2 (9)	4 (29)	67 (174)	51 (116)
LSST	7 (11)	15 (47)	51 (116)	273 (554)

mission duration in Model 1 (Model 2), while LISA can detect 16960 (32815) DWDs with SNRs greater than 7 within a 4-year nominal mission duration in Model 1 (Model 2). The number of DWDs detectable by TianQin and LISA in Model 2 is found to be twice that of in Model 1. The joint observation of TianQin and LISA can detect an additional 2,000 DWDs compared to LISA alone in Model 2. For EM observations, we found that Gaia and LSST can detect 67 (174) and 273 (554) compact eclipsing DWDs in Model 1 (Model 2) with orbital period less than 30 hours, respectively. The increased number in Model 2 is mainly due to the higher surface temperatures of the WDs generated in Model 2, making them more easily detectable by optical telescopes.

In the investigation of EM observations of eclipsing DWDs, we found that the r -band of LSST has superior performance compared to other bands, with a limiting magnitude of 24.7. The DWDs detectable by optical telescopes are predominantly distributed near the Galactic disk. Given that LSST primarily monitors the southern hemisphere, the inclusion of ZTF and other facilities in the northern hemisphere is crucial to compensate for the lack of sky coverage. In the near future, the Chinese Space Station Telescope (CSST) (Gong et al. 2019) with a g -band magnitude of 26.4 and a field of view of about 1.1 deg^2 will have the potential to conduct deeper follow-up observations and find more DWDs reported by the space-borne GW detectors. Relevant work is currently under our investigation.

For the space-borne detectors, we calculated the SNRs of DWDs for TianQin and LISA, individually and jointly. The latter can detect about 7% more DWDs compared to the LISA alone. Furthermore, we analyzed the estimation errors of the parameters using the Fisher information matrix. From the cumulative distributions of the relative errors in Figure 10, we found that the main contributions to $\Delta M/M$ and $\Delta \mathcal{D}/\mathcal{D}$ are associated with $\Delta \dot{f}/\dot{f}$ and $\Delta \mathcal{A}/\mathcal{A}$. Due to the sensitive frequencies of the GW detectors, almost all DWDs detectable by LISA and TianQin are in the range of $10^{-3} - 10^{-2}$ Hz, corresponding to orbital periods of 3-30 mins. In contrast, the orbital periods of DWDs observed in EM observations are mainly centered around one hour.

In this work, we have considered only detached DWDs in our simulated population and have produced their light curves. In the future, we will study semi-detached DWDs and simulate their EM photometric and spectroscopic signatures. Furthermore, we plan to conduct direct comparison with existing and forthcoming EM surveys of DWDs like from the Zwicky Transient Facility (ZTF; Ren et al. 2023), Gaia, the Wide Field Survey Telescope (WFST; Wang et al. 2023), and the Multi-channel Photometric Survey Telescope (Mephisto; Yuan et al. 2020), to refine our population synthesis models.

ACKNOWLEDGEMENTS

We thank Valeriya Korol, Shenghua Yu and Xiang-Dong Li for helpful discussions. HMJ is grateful for the hospitality of Nanjing University, where part of this work was done during his visit. YW gratefully acknowledges support from the National Key Research and Development Program of China (No. 2022YFC2205201, 2020YFC2201400), the National Natural Science Foundation of China (NSFC) under Grants No. 11973024, Major Science and Technology Program of Xinjiang Uygur Autonomous Region (No. 2022A03013-4), and Guangdong Major Project of Basic and Applied Basic Research (Grant No. 2019B030302001). YS acknowledges support from the National Key Research and Development Program of China (Grant Nos 2021YFA0718500 and 2023YFA1607902). BM acknowledges support from NSFC (12073092, 12103097). We acknowledge the High Performance Computing Platform at Huazhong University of Science and Technology for providing computational resources.

DATA AVAILABILITY

The simulation data underlying this article will be shared on reasonable request to the corresponding authors.

REFERENCES

- Abt H. A., 1983, *ARA&A*, **21**, 343
- Adams M. R., Cornish N. J., Littenberg T. B., 2012, *Phys. Rev. D*, **86**, 124032
- Althaus L. G., Córscico A. H., Isern J., García-Berro E., 2010, *A&ARv*, **18**, 471
- Amaral L. A., et al., 2024, *Astronomy & Astrophysics*
- Amaro-Seoane P., et al., 2017, *arXiv e-prints*, p. [arXiv:1702.00786](https://arxiv.org/abs/1702.00786)
- Amaro Seoane P., et al., 2022, *General Relativity and Gravitation*, **54**, 3
- Baker J., et al., 2019, *BAAS*, **51**, 123
- Bianco F. B., et al., 2021, *The Astrophysical Journal Supplement Series*, **258**, 1
- Breivik K., Kremer K., Bueno M., Larson S. L., Coughlin S., Kalogera V., 2018, *ApJ*, **854**, L1
- Breivik K., et al., 2020a, *The Astrophysical Journal*, **898**, 71
- Breivik K., et al., 2020b, *ApJ*, **898**, 71
- Brown W. R., Kilic M., Hermes J. J., Allende Prieto C., Kenyon S. J., Winget D. E., 2011, *ApJ*, **737**, L23
- Brown W. R., Kilic M., Kosakowski A., Gianninas A., 2017, *ApJ*, **847**, 10
- Brown W. R., et al., 2020, *ApJ*, **889**, 49
- Burdge K. B., et al., 2019, *Nature*, **571**, 528
- Burdge K. B., et al., 2020a, *ApJ*, **905**, 32
- Burdge K. B., et al., 2020b, *ApJ*, **905**, L7
- Cardelli J. A., Clayton G. C., Mathis J. S., 1989, *ApJ*, **345**, 245
- Casagrande L., VandenBerg D. A., 2018, *MNRAS*, **479**, L102
- Chen Z., Chen Y., Chen C., Ge H., Ma B., 2024, *arXiv e-prints*, p. [arXiv:2404.06845](https://arxiv.org/abs/2404.06845)
- Conroy K. E., et al., 2020, *ApJS*, **250**, 34
- Cornish N. J., Larson S. L., 2003, *Phys. Rev. D*, **67**, 103001
- Coughlin M. W., et al., 2020, *MNRAS*, **494**, L91
- Cutler C., Flanagan É. E., 1994, *Phys. Rev. D*, **49**, 2658
- D'Antona F., Mazzitelli I., 1990, *Annual Review of Astronomy and Astrophysics*, **28**, 139
- Delgado F., Reuter M. A., 2016, in Peck A. B., Seaman R. L., Benn C. R., eds, *Society of Photo-Optical Instrumentation Engineers (SPIE) Conference Series Vol. 9910, Observatory Operations: Strategies, Processes, and Systems VI*. p. 991013, [doi:10.1117/12.2233630](https://doi.org/10.1117/12.2233630)
- Delgado F., Saha A., Chandrasekharan S., Cook K., Petry C., Ridgway S., 2014, in Angeli G. Z., Dierickx P., eds, *Society of Photo-Optical Instrumentation Engineers (SPIE) Conference Series Vol. 9150, Modeling, Systems Engineering, and Project Management for Astronomy VI*. p. 915015, [doi:10.1117/12.2056898](https://doi.org/10.1117/12.2056898)
- Dewi J. D. M., Tauris T. M., 2000, *A&A*, **360**, 1043
- Dobbie P. D., et al., 2006, *MNRAS*, **369**, 383
- Dominik M., Belczynski K., Fryer C., Holz D. E., Berti E., Bulik T., Mandel I., O'Shaughnessy R., 2012, *ApJ*, **759**, 52
- Duchêne G., Kraus A., 2013, *Annual Review of Astronomy and Astrophysics*, **51**, 269
- El-Badry K., et al., 2021a, *Monthly Notices of the Royal Astronomical Society*, **505**, 2051
- El-Badry K., Rix H.-W., Heintz T. M., 2021b, *Monthly Notices of the Royal Astronomical Society*, **506**, 2269
- Finch E., et al., 2023, *MNRAS*, **522**, 5358
- Finn L. S., 1992, *Phys. Rev. D*, **46**, 5236
- Fontaine G., Brassard P., Bergeron P., 2001, *Publications of the Astronomical Society of the Pacific*, **113**, 409
- GRAVITY Collaboration et al., 2019, *A&A*, **625**, L10
- Gaia Collaboration et al., 2016a, *A&A*, **595**, A1
- Gaia Collaboration et al., 2016b, *A&A*, **595**, A2
- Gaia Collaboration et al., 2018, *A&A*, **616**, A1
- Gaia Collaboration et al., 2021, *A&A*, **649**, A1
- Gaia Collaboration et al., 2022, *arXiv e-prints*, p. [arXiv:2208.00211](https://arxiv.org/abs/2208.00211)
- Geller A. M., Leigh N. W. C., Giersz M., Kremer K., Rasio F. A., 2019, *ApJ*, **872**, 165
- Gentile Fusillo N. P., et al., 2019, *MNRAS*, **482**, 4570
- Gentile Fusillo N. P., et al., 2021a, *MNRAS*, **504**, 2707
- Gentile Fusillo N. P., et al., 2021b, *MNRAS*, **508**, 3877
- Gong Y., et al., 2019, *ApJ*, **883**, 203
- Gong Y., Luo J., Wang B., 2021, *Nature Astronomy*, **5**, 881
- Hallakoun N., et al., 2016, *MNRAS*, **458**, 845
- Han Z., 1998, *MNRAS*, **296**, 1019
- Han Z., Podsiadlowski P., Maxted P. F. L., Marsh T. R., Ivanova N., 2002, *MNRAS*, **336**, 449
- Han Z., Podsiadlowski P., Maxted P. F. L., Marsh T. R., 2003, *MNRAS*, **341**, 669
- Heggie D. C., 1975, *MNRAS*, **173**, 729
- Hermes J. J., et al., 2014, *MNRAS*, **444**, 1674
- Hirai R., Mandel I., 2022, *ApJ*, **937**, L42
- Horvat M., Conroy K. E., Pablo H., Hambleton K. M., Kochoska A., Giannarino J., Prša A., 2018, *ApJS*, **237**, 26
- Horvat M., Conroy K. E., Jones D., Prša A., 2019, *ApJS*, **240**, 36
- Hu W.-R., Wu Y.-L., 2017, *National Science Review*, **4**, 685
- Hu X.-C., et al., 2018, *Classical and Quantum Gravity*, **35**, 095008
- Huang S.-J., et al., 2020, *Phys. Rev. D*, **102**, 063021
- Hurley J. R., Tout C. A., Pols O. R., 2002, *MNRAS*, **329**, 897
- Icko Iben J., Ritossa C., Garcia-Berro E., 1997, *The Astrophysical Journal*, **489**, 772
- Ivezić Ž., et al., 2019, *ApJ*, **873**, 111
- Jiménez-Esteban F. M., Torres S., Rebassa-Mansergas A., Skorobogatov G., Solano E., Cantero C., Rodrigo C., 2018, *MNRAS*, **480**, 4505
- Jones D., et al., 2020, *ApJS*, **247**, 63
- Kaplan D. L., et al., 2014, *ApJ*, **780**, 167
- Keller P. M., Breedt E., Hodgkin S., Belokurov V., Wild J., García-Soriano I., Wise J. L., 2022, *MNRAS*, **509**, 4171
- Kilic M., et al., 2014, *Mon. Not. Roy. Astron. Soc.*, **438**, 26
- Korol V., Rossi E. M., Groot P. J., Nelemans G., Toonen S., Brown A. G. A., 2017, *Monthly Notices of the Royal Astronomical Society*, **470**, 1894
- Korol V., Rossi E. M., Barausse E., 2019, *MNRAS*, **483**, 5518
- Korol V., et al., 2020, *A&A*, **638**, A153
- Kosakowski A., Brown W. R., Kilic M., Kupfer T., Bédard A., Gianninas A., Agüeros M. A., Barrientos M., 2023, *ApJ*, **950**, 141
- Kroupa P., 2001, *MNRAS*, **322**, 231
- Kroupa P., Tout C. A., Gilmore G., 1993, *MNRAS*, **262**, 545
- Kupfer T., et al., 2018, *MNRAS*, **480**, 302
- LSST Science Collaboration et al., 2009, *arXiv e-prints*, p. [arXiv:0912.0201](https://arxiv.org/abs/0912.0201)
- LSST Science Collaboration et al., 2017, *arXiv e-prints*, p. [arXiv:1708.04058](https://arxiv.org/abs/1708.04058)
- Lamberts A., Blunt S., Littenberg T. B., Garrison-Kimmel S., Kupfer T., Sanderson R. E., 2019, *MNRAS*, **490**, 5888

- Lau M. Y. M., Mandel I., Vigna-Gómez A., Neijssel C. J., Stevenson S., Sesana A., 2020, *Monthly Notices of the Royal Astronomical Society*, 492, 3061
- Luo J., et al., 2016, *Classical and Quantum Gravity*, 33, 035010
- Marsh T. R., 2011, *Classical and Quantum Gravity*, 28, 094019
- McMillan P. J., 2011, *MNRAS*, 414, 2446
- Munday J., et al., 2023, *Monthly Notices of the Royal Astronomical Society*, 525, 1814
- Naghieb E., Yoachim P., Vanderbei R. J., Connolly A. J., Jones R. L., 2019, *AJ*, 157, 151
- Nelemans G., 2009, *Classical and Quantum Gravity*, 26, 094030
- Nelemans G., Yungelson L. R., Portegies Zwart S. F., Verbunt F., 2001a, *A&A*, 365, 491
- Nelemans G., Yungelson L. R., Portegies Zwart S. F., 2001b, *A&A*, 375, 890
- Nelemans G., Yungelson L. R., Portegies Zwart S. F., 2004, *MNRAS*, 349, 181
- Ni W. T., 1998, in Cho Y. M., Lee C. H., Kim S.-W., eds, Pacific Conference on Gravitation and Cosmology. p. 309
- Nissanke S., Vallisneri M., Nelemans G., Prince T. A., 2012, *ApJ*, 758, 131
- Parsons S. G., Marsh T. R., Gänsicke B. T., Drake A. J., Koester D., 2011, *ApJ*, 735, L30
- Peters P. C., Mathews J., 1963, *Physical Review*, 131, 435
- Portegies Zwart S. F., Verbunt F., 1996, *A&A*, 309, 179
- Postnov K. A., Yungelson L. R., 2014, *Living Reviews in Relativity*, 17, 1
- Prša A., Zwitter T., 2005, *ApJ*, 628, 426
- Prša A., et al., 2016, *ApJS*, 227, 29
- Prša A., 2018, Modeling and Analysis of Eclipsing Binary Stars. 2514-3433, IOP Publishing, doi:10.1088/978-0-7503-1287-5, <https://doi.org/10.1088/978-0-7503-1287-5>
- Ren L., Li C., Ma B., Cheng S., Huang S.-J., Tang B., Hu Y.-m., 2023, *ApJS*, 264, 39
- Renzo M., et al., 2019, *A&A*, 624, A66
- Renzo M., et al., 2021, *ApJ*, 919, 128
- Riello M., et al., 2021, *A&A*, 649, A3
- Riley J., et al., 2022, *ApJS*, 258, 34
- Robson T., Cornish N. J., Liu C., 2019, *Classical and Quantum Gravity*, 36, 105011
- Rowell N., Hambly N. C., 2011, *Monthly Notices of the Royal Astronomical Society*, 417, 93
- Ruiter A. J., Belczynski K., Benacquista M., Larson S. L., Williams G., 2010, *ApJ*, 717, 1006
- Salpeter E. E., 1955, *ApJ*, 121, 161
- Sana H., et al., 2012, *Science*, 337, 444
- Schwamb M. E., et al., 2023, *ApJS*, 266, 22
- Shao Y., Li X.-D., 2021, *ApJ*, 920, 81
- Steinfadt J. D. R., Kaplan D. L., Shporer A., Bildsten L., Howell S. B., 2010, *ApJ*, 716, L146
- Tinto M., de Araujo J. C. N., 2016, *Phys. Rev. D*, 94, 081101
- Tinto M., Debra D., Buchman S., Tilley S., 2015, Review of Scientific Instruments, 86, 330
- Toonen S., Nelemans G., Portegies Zwart S., 2012, *A&A*, 546, A70
- Toonen S., Hollands M., Gänsicke B. T., Boekholt T., 2017, *A&A*, 602, A16
- Vennes S., et al., 2011, *ApJ*, 737, L16
- Wagg T., Broekgaarden F. S., de Mink S. E., Frankel N., van Son L. A. C., Justham S., 2022, *ApJ*, 937, 118
- Wang T., et al., 2023, *Science China Physics, Mechanics, and Astronomy*, 66, 109512
- Wells M., Prša A., Jones L., Yoachim P., 2017, *PASP*, 129, 065003
- Wu J., Li J., 2023, *Phys. Rev. D*, 108, 124047
- Yu S., Jeffery C. S., 2010, *A&A*, 521, A85
- Yuan X., et al., 2020, in Marshall H. K., Spyromilio J., Usuda T., eds, Society of Photo-Optical Instrumentation Engineers (SPIE) Conference Series Vol. 11445, Ground-based and Airborne Telescopes VIII. p. 114457M, doi:10.1117/12.2562334
- Zhang F., Han Z., Li L., Hurley J. R., 2002, *MNRAS*, 334, 883
- Zhang F., Han Z., Li L., Hurley J. R., 2004, *A&A*, 415, 117
- van Haften L. M., Nelemans G., Voss R., Toonen S., Portegies Zwart S. F., Yungelson L. R., van der Sluys M. V., 2013, *A&A*, 552, A69
- van Leeuwen F., et al., 2018, Gaia DR2 documentation, European Space Agency; Gaia Data Processing and Analysis Consortium.

APPENDIX A:

Table A1. Physical properties of the known 16 eclipsing DWDs.

Source	R_1 (R_\odot)	R_2 (R_\odot)	m_1 (M_\odot)	m_2 (M_\odot)	ι ($^\circ$)	P (hour)	d (pc)	Refs.
NLTT 11748	0.0423 ± 0.0004	0.0108 ± 0.0001	0.136 ± 0.007	0.707 ± 0.008	89.67 ± 0.12	5.64	150 ± 32	1,2
CSS 41177	0.0210 ± 0.0026	0.0174 ± 0.0031	0.283 ± 0.064	0.274 ± 0.034	89.2 ± 0.3	2.78	350 ± 13	3
GALEX J1717+6757	0.101 ± 0.014	0.009	0.185 ± 0.010	0.90	86.9 ± 0.4	5.91	195 ± 7	4,5
SDSS J065133.338+284423.37	0.0371 ± 0.0012	0.0142 ± 0.001	0.247 ± 0.015	0.49 ± 0.02	$86.9^{+1.6}_{-1.0}$	0.21	1000.0 ± 100	6,7
SDSS J075141.18+014120.9	0.155 ± 0.020	0.0092 ± 0.0026	0.19	0.97 ± 0.06	$85.4^{+9.4}_{-4.2}$	1.90	1700 ± 100	8
SDSS J115219.99+024814.4	$0.0223^{+0.0064}_{-0.0050}$	0.0197 ± 0.0035	0.442 ± 0.088	0.47 ± 0.11	$89.3^{+0.140}_{-0.081}$	2.40	464^{+90}_{-85}	9
SDSS J082239.54+304857.19	$0.022^{+0.015}_{-0.014}$	$0.0041^{+0.0082}_{-0.0037}$	0.304 ± 0.014	0.524 ± 0.050	$88.1^{+1.4}_{-2.3}$	0.67	1110 ± 80	10
ZTF J153932.16 + 502738.8	$0.01562^{+0.00038}_{-0.00038}$	$0.03140^{+0.00054}_{-0.00052}$	$0.610^{+0.017}_{-0.022}$	$0.210^{+0.014}_{-0.015}$	$84.15^{+0.64}_{-0.57}$	0.12	2340 ± 140	7
ZTF J190125.42+530929.5	$0.029^{+0.001}_{-0.002}$	$0.022^{+0.003}_{-0.002}$	$0.36^{+0.04}_{-0.04}$	$0.36^{+0.05}_{-0.05}$	$86.2^{+0.6}_{-0.2}$	0.68	915^{+96}_{-80}	11,12
ZTF J053802.73+195302.89	$0.02069^{+0.0028}_{-0.00034}$	$0.02319^{+0.00032}_{-0.00026}$	$0.45^{+0.05}_{-0.05}$	$0.32^{+0.03}_{-0.03}$	$85.43^{+0.07}_{-0.09}$	0.2407	684^{+18}_{-14}	12
ZTF J202922.31+153430.97	$0.029^{+0.002}_{-0.003}$	$0.028^{+0.003}_{-0.003}$	$0.32^{+0.04}_{-0.04}$	$0.30^{+0.04}_{-0.04}$	$86.64^{+0.70}_{-0.4}$	0.3478	2020^{+150}_{-150}	12
ZTF J072221.49+183930.57	$0.0224^{+0.0004}_{-0.0002}$	$0.0249^{+0.0001}_{-0.0003}$	$0.38^{+0.04}_{-0.04}$	$0.33^{+0.03}_{-0.03}$	$89.66^{+0.22}_{-0.22}$	0.3950	928^{+23}_{-31}	12
ZTF J174955.30+092432.40	$0.022^{+0.003}_{-0.004}$	$0.025^{+0.004}_{-0.004}$	$0.40^{+0.07}_{-0.05}$	$0.28^{+0.05}_{-0.04}$	$85.45^{+1.40}_{-1.15}$	0.4405	1550^{+200}_{-180}	12
ZTF J2243+5242	$0.0298^{+0.0013}_{-0.0012}$	$0.0275^{+0.0012}_{-0.0013}$	$0.323^{+0.065}_{-0.047}$	$0.335^{+0.052}_{-0.054}$	$82.12^{+0.51}_{-0.38}$	0.1466	2425^{+108}_{-114}	13
J0225+6920	0.0291 ± 0.001	0.0244 ± 0.0007	0.4 ± 0.04	0.28 ± 0.02	85.25 ± 0.06	0.7865	$402.6^{+5.9}_{-6.8}$	14
J2102+4145	0.0211 ± 0.0002	$0.0203^{+0.0002}_{-0.0003}$	0.375 ± 0.003	0.314 ± 0.003	$88.693^{+0.006}_{-0.005}$	2.4048	165 ± 1	15,16

- [1] Kaplan et al. (2014). [2] Steinfadt et al. (2010). [3] Parsons et al. (2011). [4] Vennes et al. (2011). [5] Hermes et al. (2014). [6] Brown et al. (2011). [7] Burdge et al. (2019). [8] Kilic et al. (2014). [9] Hallakoun et al. (2016). [10] Brown et al. (2017). [11] Coughlin et al. (2020). [12] Burdge et al. (2020a). [13] Burdge et al. (2020b). [14] Munday et al. (2023) [15] Kosakowski et al. (2023) [16] Amaral et al. (2024)

This paper has been typeset from a $\text{\TeX}/\text{\LaTeX}$ file prepared by the author.